

PAPER

Effects of interlayer interactions on the nanoindentation response of freely suspended multilayer gallium telluride

To cite this article: Jin Zhang *et al* 2020 *Nanotechnology* **31** 165706

View the [article online](#) for updates and enhancements.



IOP | ebooks™

Bringing you innovative digital publishing with leading voices to create your essential collection of books in STEM research.

Start exploring the collection - download the first chapter of every title for free.

Effects of interlayer interactions on the nanoindentation response of freely suspended multilayer gallium telluride

Jin Zhang^{1,4} , Yan Zhou^{2,4}, Penghua Ying¹ , Huarui Sun¹ , Jianli Zhou¹, Tao Wang³, Wanqi Jie³ and Martin Kuball^{2,4}

¹ School of Science, Harbin Institute of Technology, Shenzhen 518055, People's Republic of China

² Center for Device Thermography and Reliability (CDTR), H. H. Wills Physics Laboratory, University of Bristol, Tyndall Avenue, Bristol BS8 1TL, United Kingdom

³ State Key Laboratory of Solidification Processing, Northwestern Polytechnical University, Xi'an 710072, People's Republic of China

E-mail: jinzhang@hit.edu.cn, yan.zhou@bristol.ac.uk and martin.kuball@bristol.ac.uk

Received 31 October 2019, revised 16 December 2019

Accepted for publication 31 December 2019

Published 31 January 2020



CrossMark

Abstract

Freestanding indentation is a widely used method to characterise the elastic properties of two-dimensional (2D) materials. However, many controversies and confusion remain in this field due to the lack of appropriate theoretical models in describing the indentation responses of 2D materials. Taking the multilayer gallium telluride (GaTe) as an example, in this paper we conduct a series of experiments and simulations to achieve a comprehensive understanding of its freestanding indentation behaviours. Specifically, the freestanding indentation experiments show that the elastic properties of the present multilayer GaTe with a relatively large thickness can only be extracted from the bending stage in the indentation process rather than the stretching stage widely utilised in the previous studies on thin 2D materials, since the stretching stage of thick 2D materials is inevitably accompanied with severe plastic deformations. In combination with existing continuum mechanical models and finite element simulations, an extremely small Young's modulus of multilayer GaTe is obtained from the nanoindentation experiments, which is two orders of magnitude smaller than the value obtained from first principles calculations. Our molecular dynamics (MD) simulations reveal that this small Young's modulus can be attributed to the significant elastic softening in the multilayer GaTe with increasing thickness and decreasing length. It is further revealed in MD simulations that this size-induced elastic softening originates from the synergistic effects of interlayer compression and interlayer shearing in the multilayer GaTe, both of which, however, are ignored in the existing indentation models. To consider these effects of interlayer interactions in the theoretical modelling of the freestanding indentation of multilayer GaTe, we propose here novel multiple-beam and multiple-plate models, which are found to agree well with MD results without any additional parameters fitting and thus can be treated as more precise theoretical models in characterising the freestanding indentation behaviours of 2D materials.

Supplementary material for this article is available [online](#)

Keywords: two-dimensional materials, nanoindentation testing, elastic properties, indentation models, interlayer interactions

(Some figures may appear in colour only in the online journal)

⁴ Authors to whom any correspondence should be addressed.

1. Introduction

The successful isolation of monolayer graphene by the mechanical exfoliation of bulk graphite in 2004 [1] has pushed forward the development of two-dimensional (2D) materials. Besides graphene, many other 2D materials such as boron nitride (BN), molybdenum disulphide (MoS_2), silicene, black phosphorus and so on have been discovered to date [2–6]. Existing theoretical and experimental studies show that most of these 2D materials possess unique properties superior to their bulk counterparts [6, 7]. For example, excellent mechanical properties such as ultrahigh in-plane stiffness and strength but extremely low flexural rigidity have been detected in many 2D materials, which render them appealing in applications of flexible transistors, resonators, oscillators and sensors [8–10]. In addition to playing a key role in designing novel 2D devices, mechanical properties are also key factors determinately affecting the strain engineering of 2D materials, which provides a promising way to efficiently modulate the physical properties such as electronic and optical properties of 2D materials [11, 12]. Thus, investigating the mechanical behaviours especially the elastic properties of 2D materials not only promotes the future applications of 2D materials in novel nanodevices, but also helps to better know about other physical properties of 2D materials.

In recent decade years, numerous characterisation methods have been developed to identify the elastic properties of 2D materials, which include experimental and computational techniques. Specifically, in computational studies both molecular dynamics (MD) simulations and first principles calculations are widely employed [8–10]. Meanwhile, abundant experimental methods such as indentation testing [13–15], *in situ* tensile testing [16, 17] and dynamic measurement [18, 19] have been proposed to measure the elastic properties of 2D materials. Among various experimental methods, the indentation of freestanding 2D materials or the freestanding indentation testing is one of the mostly utilised techniques [8–10, 15, 17]. This method not only can be easily implemented at the nanoscale, but also has the ability to avoid both the non-uniformity of strain and the defect-initiated breaking from edges usually occurring in the conventional tensile testing of thin films [15, 20, 21]. On the other hand, some unusual elastic properties of 2D materials observed recently in the freestanding indentation tests bring some controversies and confusion in this method. For example, the Young's modulus of many 2D materials measured by freestanding indentation testing is found to be strongly dependent on the size of materials. Specifically, most of these 2D materials such as graphene [22–25], graphene oxide [26], BN [27], MoS_2 [28], gallium sulphide [29], gallium telluride (GaTe) [19], black phosphorus [30] and 2D hybrid organic–inorganic perovskites [31] possess a Young's modulus declining as the thickness increases but growing as the length increases. Moreover, the freestanding indentation testing sometimes produces a Young's modulus extraordinarily smaller than the value extracted from some precise quantum mechanics calculations. For instance, the Young's modulus of BN nanosheets obtained from the freestanding indentation

experiments is around 18 GPa [27], which is greatly smaller than the result of 952 GPa extracted from density functional theory (DFT) calculations [32]. It is known that, in order to obtain the Young's modulus of a 2D material through the freestanding indentation testing one should employ an equivalent analytical model to fit the measured load–displacement curve. Thus, the accuracy of the selected analytical model plays a key role in precisely archiving the elastic properties of 2D materials. In most existing studies, the conventional beam and plate models are directly used to describe the indentation behaviours of freestanding 2D materials by tacitly ignoring their nanoscale characteristics. However, different from their three-dimensional crystalline counterparts possessing chemical bonds in three directions, 2D materials usually have a layered structure, which consists of strong chemical bonds in each layer but weak van der Waals (vdW) interactions between neighbouring layers. This special crystal structure especially the weak interlayer interactions may make the 2D materials exhibit some unique mechanical behaviours different from those of their conventional three-dimensional crystalline counterparts. Under this circumstance, it is of great importance to achieve a comprehensive understanding of the effects of interlayer interactions on the nanoindentation response of freestanding 2D materials.

The layered GaTe is an important member of the 2D material family, which attracts great interests very recently because of its promising electronic and optoelectronic properties [19, 29, 33–35]. In this paper, the nanoindentation response of the freely suspended multilayer GaTe nanosheets is investigated by using a method combining experimental testing, computational simulations and theoretical modelling. Specifically, the nanoindentation experiments are conducted to obtain the indentation load-indentation depth relationship of GaTe nanosheets. The obtained experimental results are subsequently utilised to calculate the Young's modulus of multilayer GaTe with the aid of the existing continuum mechanical models and finite element (FE) simulations. The Young's modulus extracted from the experiments is found to be significantly smaller than the value obtained from first principles calculations. **This difference is well explained by MD simulations, which can be attributed to the synergistic effects of the interlayer compression and interlayer shearing existing in the multilayer GaTe. Taking into account these effects of interlayer interactions in the theoretical modelling, we develop here a new continuum mechanical model, which is found to have the ability to more precisely describe the freestanding indentation behaviours of multilayer GaTe nanosheets.**

2. Freestanding indentation experiments of multilayer GaTe nanosheets

The single-crystal bulk GaTe ingot was grown by the modified vertical Bridgeman method. During the crystal growth process, the accelerated crucible rotation technique was exploited to improve the mass and heat transport and, meanwhile, to smooth the solid-liquid interface. High purity

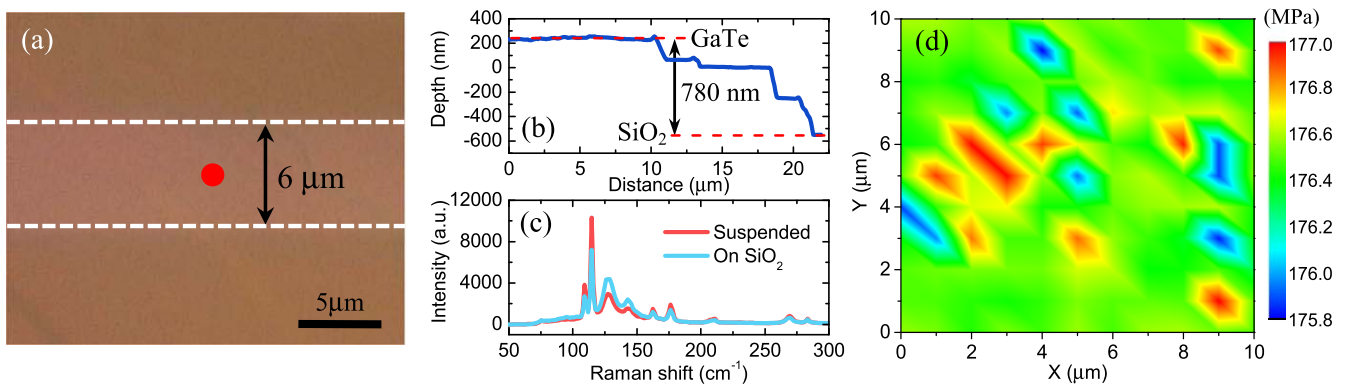


Figure 1. Identification and characterisation of the freely suspended multilayer GaTe nanosheets. (a) Optical microscopy image of a GaTe nanosheet laying on the SiO₂ substrate with trench patterns having a 6 μm width and a 300 nm depth. Here, the region between two dashed lines is the freely suspended GaTe nanosheets, while the others are GaTe nanosheets laying on the substrate. (b) Line-scan profile on the edge region of the GaTe nanosheet, indicating that the GaTe nanosheet has a uniform thickness around 780 nm. (c) Raman spectrum of a freely suspended GaTe nanosheet. The suspended region in the GaTe nanosheets and the region supported on substrate both are measured. (d) Distribution of the residual stress in freely suspended GaTe nanosheets.

powders of gallium (99.99%, Alfa Aesar) and telluride (99.99%, Alfa Aesar) with chemical stoichiometry were mixed in a rocking synthesise furnace and sealed in an evacuated quartz ampoule ($<10^{-4}$ Torr vacuums). Single-crystal GaTe wafers in a dimension of $\sim 15 \times 15 \times 2$ mm³ were cut from the above GaTe ingot. The GaTe multilayers were mechanically exfoliated from the single-crystal bulk GaTe wafer onto 300 nm SiO₂/Si substrates using the Scotch tape as the transfer medium. It is noted here that, to better study the effects of interlayer interactions on the nanoindentation behaviours of multilayer GaTe nanosheets, relatively thick GaTe nanosheets possessing more interlayers were fabricated, which are in contrast to the ultrathin GaTe nanosheets with only a few layers employed in the previous studies [19, 29]. Moreover, in order to create the freely suspended multilayer GaTe nanosheets for the nanoindentation tests, trench patterns with a 6 μm width and a 300 nm depth were fabricated on the SiO₂/Si substrates by photolithography and reactive ion etching. Moreover, before exfoliating the substrates were cleaned in sequence in acetone, ethanol and de-ionised water, and subsequently followed by the oxygen plasma treatment to remove ambient adsorbates on the surface.

In figure 1(a) we show the optical microscopy image of GaTe nanosheets after being transferred onto the substrate with pre-fabricated trench patterns. Specifically, the region between two dashed lines in figure 1(a) is the freely suspended GaTe, while the others are the GaTe laying on the SiO₂ substrate. The exfoliated GaTe nanosheets have a length around 40 μm, which can be directly detected from the optical microscopy image. The thickness of the GaTe nanosheets was measured by using atomic force microscopy (AFM) scans in the tapping mode. It is noted that due to the existence of defects and preferred cleavage plane in the single-crystal multilayer GaTe, region-to-region variations in thickness may exist in the exfoliated GaTe nanosheets. This variation in thickness becomes more pronounced in the thicker GaTe nanosheets, but many relatively large flat surface regions can still be obtained. Considering such thickness variation of the

exfoliated GaTe nanosheets, their exact thickness was accurately measured by AFM according to their relative height to the SiO₂ substrate. According to the obtained topography mappings shown in figure 1(b), the thickness of the exfoliated GaTe nanosheets is about 780 nm. Moreover, our x-ray diffraction pattern and transmission electron microscope analyses (figures S1 and S2 in the supplementary materials are available online at stacks.iop.org/NANO/31/165706/mmedia) both show that the exfoliated multilayer GaTe possesses a monoclinic crystal structure. In figure 1(c) we show the Raman spectra of the freely suspended GaTe nanosheet and its counterpart supported on the SiO₂ substrate. Here, the Raman measurements were performed with the Renishaw InVia Raman instrument at the room temperature using an Ar⁺ laser (488 nm) with an incident power of ~ 0.25 mW and a spot size of ~ 1 μm. From figure 1(c) we can observe five A_g modes (109, 114, 209, 268, 283 cm⁻¹), two B_g modes (162, 175 cm⁻¹), and two double-resonant modes (128, 143 cm⁻¹) existing at the freshly exfoliated samples, which is exactly similar to the results previously reported for the multilayer GaTe flakes [34, 36, 37]. Moreover, figure 1(c) also clearly shows that no detectable frequency differences are observed in A_g, B_g and double-resonant modes of the supported and suspended GaTe nanosheets, which indicates that the supported and suspended regions in the GaTe nanosheets have the similar prestress state. It is known that in the nanoindentation experiments of the freestanding 2D materials the prestress intrinsically existing in them is a key factor significantly affecting their measured elastic properties, which is thus worth an accurate identification. In the previous studies [13, 14, 19, 21, 23, 26, 28–31, 38] the prestress was usually obtained by fitting a continuum mechanical model to the experimental data. As a result, the accuracy of the obtained prestress strongly relies on the reliability of the chosen continuum mechanical models. Here, the prestress in the multilayer GaTe nanosheets and its distribution were directly obtained through measuring the Raman shifts of typical Raman modes. The obtained prestress distribution in the GaTe nanosheets is shown in figure 1(d). We can see from

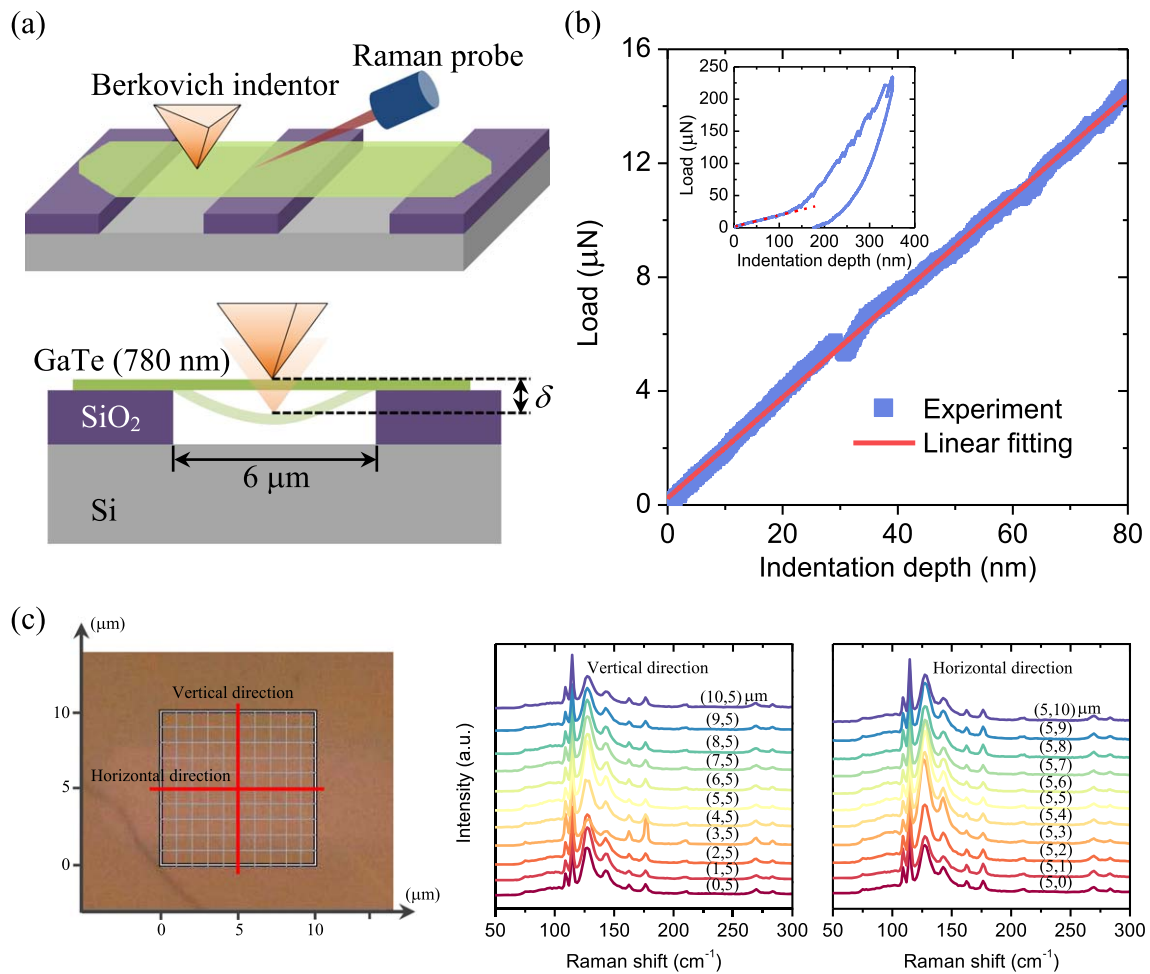


Figure 2. Freestanding indentation test for the multilayer GaTe nanosheets. (a) Perspective and side views of the schematic diagram illustrating the nanoindentation measurement carried out on the freely suspended GaTe nanosheets. (b) Load–displacement curve of the GaTe nanosheets indented by a relatively small load. The inset shows the result of the GaTe nanosheets indented by a relatively large load. Obvious pop-in, load-drop, and push-out phenomena are observed in the nonlinear region of the load–displacement curve, which denotes that severe plastic deformations occurring in this nonlinear region. (c) Micro-Raman spectra evolution along the vertical direction and horizontal direction of the mapping area in the indented GaTe nanosheets.

figure 1(d) that only the residual tensile stress exists in the multilayer GaTe nanosheets, which is in accordance with the previous reports [29, 38]. Moreover, different regions in the exfoliated GaTe nanosheets are found to possess different prestresses in magnitude, but this difference is extremely small. The average prestress in the present multilayer GaTe nanosheets is around 176 MPa, which is found to have the same order of magnitude as that of their graphene and graphene oxide counterparts [13, 39].

To investigate the elastic properties of the freely suspended multilayer GaTe nanosheets, nanoindentation testing (Hysitron TI 980 Nanoindenter) was performed. In doing this, as shown in figure 2(a), a three-pointed pyramid diamond Berkovich indenter with a 65.3° face angle and a ~ 20 nm tip radius was used to generate a series of indents with different indentation depths on the sample under the displacement control mode. Specifically, the indenter was located in the centre of the freely suspended GaTe nanosheets (the red dot in figure 1(a)). According to the previous studies [15, 40], as for the present nanoindentation experiment with a relatively large

ratio of sample size to indenter tip radius (the ratio is around 150), the nanoindentation response is not sensitive to the tip radius. Thus, in the present study the Berkovich indenter can be treated as a point load. Meanwhile, as shown in figure 2(a), the Raman measurements were also employed to monitor the possible crystal structural changes of the multilayer GaTe during the nanoindentation testing process. To avoid any possible complicated plastic deformations occurring during the indentation process, the indentation depth (i.e. δ shown in figure 2(a)) is no more than 80 nm. The indentation load as a function of the indentation depth obtained from the freestanding nanoindentation experiments is graphically shown in figure 2(b). The indentation load is found to linearly increase as the indentation depth grows, which indicates that the nonlinear elasticity and the plasticity are trivial in this nanoindentation testing with a relatively small indentation depth, and thus the strain generated in the indented GaTe nanosheets mainly originates from the linear elastic deformations. In figure 2(c) we show the Raman spectra evolution along the cross-trench direction (i.e. the vertical direction) and

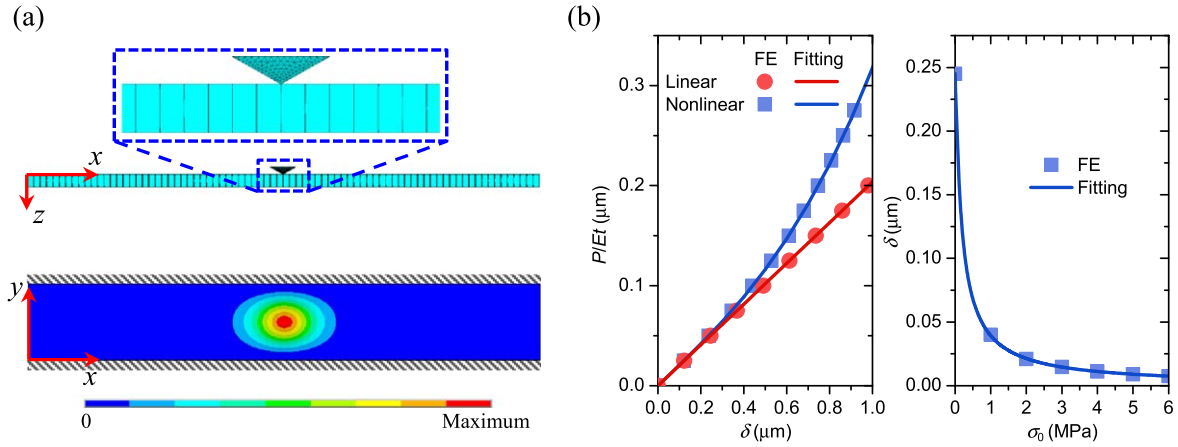


Figure 3. FE simulations on the nanoindentation of the freely suspended GaTe nanosheets. (a) FE simulation model and the simulated deformations of the GaTe nanosheet after an indentation load is applied. (b) Displacement of the centre in the GaTe nanosheets after different indentation loads and pretensions are applied. The obtained FE results are fitted by the existing plate models (equation (1)) to identify the unknown parameters in them.

the parallel-trench direction (i.e. the horizontal direction) of the GaTe nanosheets after the indentation. No significant changes are observed in the Raman spectra of the GaTe nanosheets before and after indentation, which indicates that there are no significant plastic deformations (or crystal structural changes) occurring in the GaTe nanosheets during the nanoindentation testing process.

In order to extract the Young's modulus of GaTe nanosheets from the experimental data obtained in the nanoindentation tests, following the previous studies [15, 27], we employed the pre-stretched rectangle plate model, which is clamped at two opposite edges and is under a centrally concentrated load. Based on this plate model, the indentation load P and the indentation depth δ have the following relationship [15]

$$P = \left(A \frac{Et^3}{L^2} + B\sigma_0 t \right) \delta + C \frac{Et}{L^2} \delta^3, \quad (1)$$

where E is the Young's modulus, σ_0 is the prestress, t and L are the thickness and length, and A , B and C are dimensionless parameters mainly determined by the width-to-length ratio of the plate [27, 41]. The three terms on the right-hand side of equation (1) are, respectively, associated with the bending, the pretension and the mid-plane stretching in the plate. Usually, it is extremely difficult to obtain the analytical expressions of parameters A , B and C . They can be determined by using FE simulations.

The present FE simulations were conducted by using the commercial code ANSYS. In this process, as shown in figure 3(a), the indenter was modelled by SOLID185 elements, while the GaTe nanosheet having the same geometric size as that considered in the above nanoindentation experiments was described by SHELL181 elements. The Young's modulus of the GaTe nanosheet was tacitly assumed to be 1 GPa. After indenting the nanosheet by contacting the indenter to the centre of the nanosheet, we find in figure 3(a)

that the deflection of the nanosheet has a maximum value at the central contacted region, which, however, decays along both the length and the width directions. In figure 3(b) we show the maximum deflection (or the indentation depth δ) of the nanosheet without pretension when different indentation loads (measured by the parameter P/Et) are applied. In the present FE calculations both linear and nonlinear solvers were employed. As expected, under a relatively large indentation load, the indentation depth of the nonlinear model is smaller than that of its linear counterpart. This difference is found to increase as the indentation load increases. Here, the linear results were utilised to identify parameter A , while the nonlinear results were adopted to determine parameter C . To achieve the value of parameter B , we applied different pretensions to the nanosheet when the indentation load (P/Et) was fixed at $0.5 \mu\text{m}$. The indentation depth is graphically shown in figure 3(b) as a function of the pretension, which is found to significantly decrease as the pretension increases. By fitting equation (1) to the FE results shown in figure 3(b) we can obtain the values of parameters A , B and C , which are 11.47, 1.07 and 4.10, respectively. Thus, from equation (1) we can see that, as for the nanosheets under an indentation depth smaller than 80 nm the bending term in equation (1) is much larger than the mid-plane stretching term, which results in a linear relationship between the indentation load and the indentation depth. This result is in good accordance with the above experimental observations. Furthermore, by fitting equation (1) to the experimental data shown in figure 2(b), we find that the Young's modulus of the multilayer GaTe nanosheets extracted from the freestanding indentation tests is around 0.20 GPa.

It is noted here that the Young's modulus of the multilayer GaTe obtained from the present freestanding indentation testing is associated with the bending of the structures (i.e. the first term in equation (1)). In the previous freestanding indentation studies of 2D materials with one layer or just a

few layers, the mid-plane stretching (i.e. the third term in equation (1)) rather than the bending deformation was used to determine the Young's modulus. However, this method is inapplicable for relatively thick 2D materials such as the multilayer GaTe nanosheets considered here. It is known that, to trigger the significant mid-plane stretching deformation in the thick freestanding 2D materials, one should indent these materials by an extremely large indentation depth, which may induce severe plastic deformations in this process. In the inset of figure 2(b), we show the indentation depth-indentation load curve extracted from the 350 nm depth indentation of our freely suspended multilayer GaTe samples. We find that the indentation load linearly increases as the indentation depth grows initially, which indicates that the bending plays a dominant role in the deformation of the nanosheets at the beginning stage of the indentation testing process. If we keep increasing the indentation depth, a significant nonlinear relationship is observed between the indentation depth and the indentation load, which denotes that the effect of the mid-plane stretching becomes dominant. However, in the nonlinear region the indentation depth-indentation load curve is accompanied with many pop-in, load-drop, and push-out phenomena, which are induced by the plastic deformations in the indented GaTe nanosheets. Indeed, after we completely remove the indentation load, an irreversible plastic deformation about 170 nm is retained in the GaTe nanosheets. **The significant plastic deformations occurring in the indented GaTe nanosheets are out of reach of any existing elastic models.**

3. First principles calculations of the elastic properties of monolayer and multilayer GaTe

To verify the accuracy of the Young's modulus of the multilayer GaTe obtained from the above freestanding indentation testing, we also calculated the Young's modulus of monolayer and multilayer GaTe nanosheets (layer count ranges from 1 to 6) from the first principles calculation, which is a precise simulation method based on the quantum mechanics. It is noted that, although the multilayer GaTe considered in our nanoindentation experiments has a monoclinic crystal structure, recent theoretical and experimental studies [35–37] prove that the monoclinic structure with the C2/m space group and the hexagonal structure with the P6₃/mmc space group can both stably exist in the GaTe nanosheets (see figure 4(a)), which depends on the thickness of GaTe nanosheets. Specifically, the GaTe nanosheets with a small thickness (or only a few layers) tend to possess a hexagonal structure, while in the GaTe nanosheets with a relatively large thickness the monoclinic structure is often observed [36]. Thus, both monoclinic and hexagonal structures of GaTe nanosheets were considered in our calculations.

All first principles calculations conducted here were based on DFT and were implemented by using the CASTEP code, which is a calculation programme based on DFT using a plane wave instead of an electron wave function [42]. In the calculations we adopted the generalised gradient approximation

functional in the framework of the Perdew–Burke–Ernzerhof [43] for the exchange–correlation effects. Meanwhile, the dispersion corrected method (DFT-D2) proposed by Grimme [44] was also employed to better deal with the vdW interactions in the multilayer GaTe. The structural relaxation process was firstly conducted. In this process, a 10 × 22 × 1 Monkhorst–Pack *k*-grid mesh was used for the unit cell of the hexagonal GaTe, while a 13 × 13 × 1 Monkhorst–Pack *k*-grid mesh was used for its monoclinic counterpart. The structural optimisation relaxation was finalised until the energy difference was converged within 10^{−6} eV together with a Hellman–Feynman force convergence threshold of 10^{−4} eV Å^{−1}. A periodic boundary condition was applied with a vacuum region of 20 Å along the thickness direction to avoid the mirror interactions between adjacent images. Afterwards, in calculating the elastic response of GaTe crystals, the unit cell shown in figure 4(a) (the dashed rectangular) was gradually expanded along one in-plane direction. It is noted that, due to the Poisson effect, stretching GaTe crystals along one direction will also generate deformations in the perpendicular direction. Under this circumstance, in order to guarantee the uniaxial loading condition, in the present simulations the unit cell size in the direction perpendicular to the loading was changed consequently to eliminate stresses in the perpendicular direction [45]. The strained unit cell of the GaTe crystal was thus relaxed into its minimum potential energy configuration. A series of simulations were performed to continuously expand the unit cell, resulting in a continuous stress–strain curve of the strained unit cell. The stress in the deformed GaTe nanosheets was calculated from CASTEP after defining their effective thickness as [38] $t = nd$, where n is the layer count and d is the interlayer spacing. Here, the interlayer spacing of the multilayer GaTe extracted from the present DFT calculations is, respectively, 7.6 Å for the monoclinic structure and 8.8 Å for its hexagonal counterpart (see figure 4(a)). These results are found to agree well with the values reported in the previous studies [37]. The Young's modulus was thus extracted from the linear elastic regime in the obtained stress–strain curve under a small strain. Here, the unit cell of the GaTe crystal was expanded in both x (armchair) and y (zigzag) directions to investigate the dependence of the elastic properties of GaTe nanosheets on their crystal orientation.

In figure 4(b) we show the Young's modulus of both hexagonal and monoclinic structures of the GaTe nanosheets with different layer counts. An isotropic Young's modulus is observed in the hexagonal GaTe nanosheets. However, the Young's modulus in the armchair direction of the monoclinic GaTe nanosheets is found to be much smaller than that in their zigzag direction. The smaller Young's modulus existing in the armchair direction of the monoclinic GaTe nanosheets can be attributed to the fact that, in this direction their unit cells are only connected by some single gallium–gallium bonds, while in the zigzag direction the bonding is more complex. Moreover, we also find from figure 4(b) that the Young's modulus of both hexagonal and monoclinic GaTe nanosheets is almost independent with the layer count. Specifically, the Young's modulus of the hexagonal GaTe nanosheets is found to be around 61.1 GPa when the layer count increases from 1 to 6. The

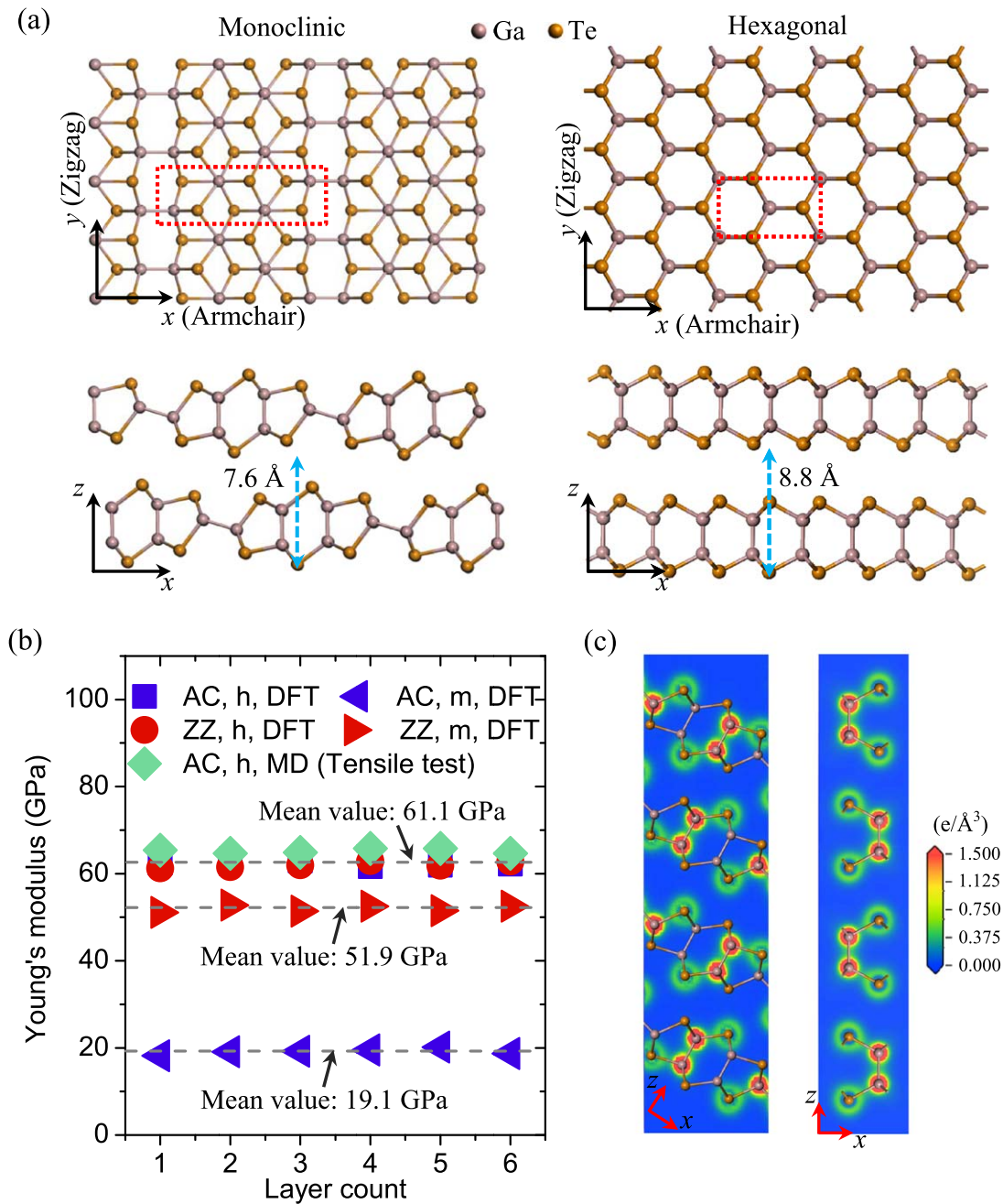


Figure 4. Elastic properties of the multilayer GaTe obtained from DFT calculations. (a) Top and side views of the structural models of the monoclinic and hexagonal GaTe. The dashed line denotes the primitive cell used in DFT calculations. The x direction of the orthogonal coordinate system corresponds to the armchair direction, while the y direction corresponds to the zigzag direction. (b) The Young's modulus in the armchair (abbreviated by AC) and zigzag (abbreviated by ZZ) directions of the monoclinic (abbreviated by m) and hexagonal (abbreviated by h) GaTe nanosheets with different layer counts. (c) Valence electron densities of the quadruple-layered monoclinic and hexagonal GaTe.

Young's modulus of the hexagonal GaTe nanosheets extracted from the present DFT calculations is consistent with the result of 60.77 GPa reported in the previous DFT calculations on hexagonal GaTe monolayers [46]. As the layer count increases from 1 to 6, the Young's modulus of the monoclinic GaTe nanosheets is around 19.1 GPa in the armchair direction and around 51.9 GPa in the zigzag direction. To understand the independence of the Young's modulus of the multilayer GaTe on the layer count, in figure 4(c), as an example, we show the charge

density distributions of the quadruple-layered monoclinic and hexagonal GaTe nanosheets. It is clearly found that there is no overlap of electronic cloud between atoms in two neighbouring component layers in the GaTe nanosheets, which denotes that the interaction between component layers in the GaTe nanosheets is in the vdW range. The existence of weak vdW interaction between the component layers in the GaTe nanosheets can be further proven by the electronic localisation function of multilayer GaTe shown in figure S3 (see the supplementary

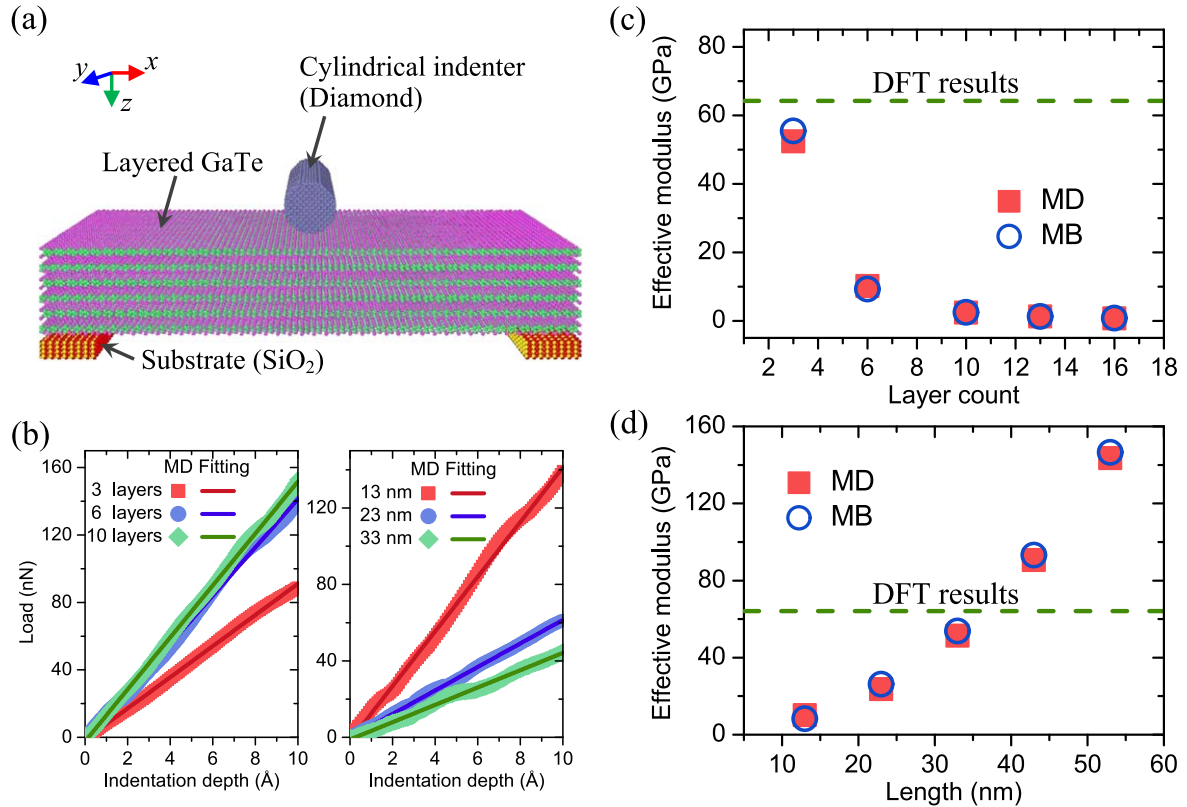


Figure 5. Nanoindentation simulations of the freely suspended GaTe nanosheets based on MD. (a) Schematic of the nanoindentation simulation using a cylindrical indenter tip. (b) Load–displacement curve of the indented GaTe nanosheets with different layer counts and lengths. Here, the MD results are fitted by the existing continuum mechanical model (equation (2)) to extract the effective Young’s modulus. (c), (d) The effective Young’s modulus extracted from the MD-based nanoindentation simulations as a function of the layer count and the length of GaTe nanosheets. For the sake of comparison, values obtained from the MB model proposed here are also presented.

materials). Thus, if we simultaneously stretch every component layer in the GaTe nanosheets along the same in-plane direction, the weak vdW interaction between component layers in the GaTe nanosheets will have a trivial influence on their tensile properties such as the Young’s modulus studied here. Different to their Young’s modulus, the electronic properties of the GaTe nanosheets, however, are found to be strongly dependent on their layer count. As shown in figure S4 in the supplementary materials, GaTe nanosheets having a smaller layer count are found to possess a wider band gap. This observation is consistent with the previous first principles studies on the electronic properties of multilayer GaTe [33, 47, 48].

The Young’s modulus of monoclinic GaTe nanosheets obtained from DFT calculations ranging from 19.1 to 51.9 GPa is in great contrast with the value of 0.20 GPa extracted from the above freestanding indentation testing. Actually, in terms of the Young’s modulus of 2D materials, a significant difference between freestanding indentation tests and DFT calculations is also observed in the previous studies on multilayer BN nanosheets [27]. The significant difference between the Young’s moduli of 2D materials extracted from freestanding indentation tests and DFT calculations suggests that it is essential to conduct a deep analysis of the freestanding indentation tests of 2D materials and also verify the accuracy of the existing continuum

mechanical models in describing their indentation responses. Motivated by this idea, we present below detailed analyses based on MD simulations.

4. MD simulations of the freestanding indentation of GaTe nanosheets

The freestanding indentation behaviours of multilayer GaTe nanosheets were simulated by MD simulations in this section. Here, the relatively thin GaTe nanosheets with a layer count ranging from 3 to 16 were considered in the present study. As we mentioned above, the GaTe nanosheets with a relatively small thickness favourably possess a hexagonal crystal structure [36]. Under this circumstance, all GaTe nanosheets considered in MD simulations have a hexagonal structure. As shown in figure 5(a), in the present simulations the freely suspended GaTe nanosheets were created by placing two opposite ends of a rectangle GaTe nanosheet on the substrates modelled by two SiO₂ blocks. Moreover, to simplify our analysis without losing generality, in MD simulations we selected a cylindrical indenter tip (shown in figure 5(a)) instead of the pyramidal indenter tip utilised in the above experiments, which can simplify the indentation stress field in the 2D GaTe

and thus facilitate the analysis of its intrinsic indentation response [20, 49]. A similar cylindrical indenter tip was also widely utilised in the previous MD simulations on the nanoindentation of graphene sheets [20, 49]. In the present simulations, the indenter tip was modelled by carbon atoms, which were uniformly distributed in a solid cylinder having a radius of 5 Å and following a diamond cubic lattice structure (to simulate the diamond indenter tip used in real tests). The axis of the cylinder is parallel to the lateral direction (i.e. y direction in figure 5(a)) of the rectangle GaTe samples and locates above the middle of the GaTe nanosheets.

In the present MD simulations, the interactions among gallium and tellurium atoms in each hexagonal GaTe layer were described by the Stillinger–Webber (SW) potential [50]. The SW potential together with the potential parameters suggested in [51] is proven to have the ability to describe the mechanical behaviours of hexagonal GaTe nanosheets well [51]. The interaction between carbon atoms in the cylindrical diamond indenter tip was described by the adaptive intermolecular reactive empirical bond-order (AIREBO) potential [52], while the interactions of silicon–silicon, silicon–oxygen, and oxygen–oxygen in the SiO₂ substrates were described by the Tersoff potential [53]. Here, values of the potential parameters in the AIREBO and Tersoff potentials were, respectively, adopted from [52, 54]. Considering the fact that the adjacent layers in GaTe nanosheets, the indenter tip and the uppermost GaTe layer, the SiO₂ substrate and the lowermost GaTe layer were all interacted through the long-range vdW force, the Lennard-Jones (LJ) 12-6 potential was utilised to describe these vdW interactions. Here, the LJ parameters were taken from [55–57] for GaTe–GaTe, GaTe–C and GaTe–SiO₂ interactions, respectively. The values of these LJ parameters are listed in the supplementary materials (table S1). All MD simulations were conducted using the open-source software LAMMPS [58]. The periodical boundary condition was applied along the lateral direction (y direction) to exclude the lateral edge effect of GaTe nanosheets. The present MD simulations on the nanoindentation testing of GaTe nanosheets were implemented in the following procedure. First, we applied the conjugate gradient algorithm to the initially constructed structures, which results in the energy-minimised configurations of these structures. Second, we completely relaxed the obtained locally energy-minimised system under the room temperature (300 K) for a certain period to make the system reach its equilibrium state. Here, the equilibrium state of this system was obtained within the NVT ensemble (constant number of particles, volume, temperature) with the aid of the velocity Verlet algorithm to update the positions and velocities of atoms. Meanwhile, the Nosé–Hoover temperature thermostat [59] was utilised to maintain the system at a constant temperature. Third, we froze the atoms in SiO₂ substrates by setting their velocities and forces to be zero and, meanwhile, moved downward the atoms in the indenter tip by a relatively small incremental displacement. In this process, we chose a relatively low loading rate of 0.05 Å ps⁻¹ to avoid the crystalline defects

normally produced due to a high rate of loading. Last, we fixed the atoms in the indenter tip and relaxed the system again to allow the GaTe nanosheets reach a new equilibrium state. By repeating the last two steps described above, we can continuously indent the GaTe nanosheets until the required indentation depth has been obtained.

From the nanoindentation simulations illustrated above, in figure 5(b) we show the obtained indentation load-indentation depth curves of the GaTe nanosheets with the same width (8 nm) but different layer counts and different lengths. Since a relatively small indentation depth which is no more than 10 Å was considered in all nanoindentation simulations, all indentation load-indentation depth curves show that the indentation load in the indented GaTe nanosheets nearly linearly increases as the indentation depth increases, irrespective of their layer count and length. However, the GaTe nanosheets with different layer counts and lengths have different indentation responses. Specifically, under the same indentation depth, the GaTe nanosheets having a larger layer count or a smaller length tend to possess a larger indentation load.

The GaTe nanosheets considered in the present nanoindentation simulations, which were indented by using a cylindrical indenter tip usually can be described by a doubly clamped beam. Under this circumstance, the relationship between the indentation load P and the indentation depth δ can be analytically expressed as [15, 60]

$$P = \left[\frac{\pi^4 E w}{6} \left(\frac{t}{L} \right)^3 + \frac{\pi^2 T}{2L} \right] \delta + \frac{\pi^4 E w t}{8} \left(\frac{\delta}{L} \right)^3, \quad (2)$$

where w is the beam width and T denotes the pre-tension. Since linear P – δ curves under a small δ are obtained in the present nanoindentation simulations, the third term on the right-hand side of equation (2) representing the mid-plane stretching effects can be ignored. Moreover, because the GaTe nanosheets considered in the present nanoindentation simulations are intrinsically perfect without any initial defects, no significant residual stresses are observed in the GaTe nanosheets. As a result, the second term in equation (2) representing the pre-tension effect also can be ignored. Thus, only the first term in equation (2) remains, which denotes that the strains generated in the indented GaTe nanosheets mainly originate from their bending deformations. The linear relationship between P and δ observed in equation (2) (only the first term remains) is in consistence with the linear P – δ curves obtained in the MD-based nanoindentation simulations. Thus, by fitting equation (2) to the MD results shown in figure 5(b) we can achieve the effective Young's modulus of the GaTe nanosheets considered in the nanoindentation simulations.

In figure 5(c) we show the effective Young's modulus of the GaTe nanosheets whose layer count changes from 3 to 16. Here, all GaTe nanosheets have the same length of 33 nm. From figure 5(c) we can see that the effective Young's modulus of GaTe nanosheets extracted from the nanoindentation simulations decreases as their layer count increases. For example, when the layer count of the GaTe nanosheets increases from 3 to 16, their Young's modulus is found to decrease from 52.3 GPa to

0.72 GPa. A similar decrease in the Young's modulus with increasing thickness (or increasing layer count) was also observed in many previous freestanding indentation experiments and simulations of various 2D materials such as graphene [22–25], BN [27], black phosphorus [30], MoS₂ [28], gallium sulphide [29] and 2D hybrid organic–inorganic perovskites [31]. In addition to the layer count, the effective Young's modulus of GaTe nanosheets obtained from the present nanoindentation simulations is also found to strongly depend on the length of nanosheets. In figure 5(d) we show the obtained effective Young's modulus of triple-layered GaTe nanosheets with a length ranging from 13 to 53 nm. When the length of the GaTe nanosheets increases from 13 to 53 nm, their Young's modulus is found to grow from 10.1 to 143.5 GPa. The increase in the Young's modulus with increasing length observed in the present nanoindentation simulations of GaTe nanosheets was similarly found in the freestanding indentation experiments of many other 2D materials such as graphene oxide nanosheets [26]. From the above obtained results we can come to the conclusion that the effective Young's modulus of GaTe nanosheets extracted from the freestanding indentation testing tends to strongly depend on their thickness and length. Specifically, a GaTe nanosheet with a larger thickness (or layer count) and a smaller length tends to possess a smaller Young's modulus. This conclusion can be employed to explain the extremely small Young's modulus observed in the above freestanding indentation experiments of the thick and short GaTe nanosheets.

The abnormal size dependence of the Young's modulus observed in the multilayer GaTe nanosheets is not induced by the SW potential selected here in describing the GaTe nanosheets, because if we calculate the Young's modulus of the GaTe nanosheets in MD simulations directly through the tensile testing rather than the nanoindentation testing, the obtained Young's modulus is found to be independent with the layer count and, meanwhile, quantitatively agrees well with the DFT results (see figure 4(b)). Details on the MD-based tensile testing conducted here are illustrated in the supplementary materials. Thus, to further shed some lights on the mechanism behind the size-dependent Young's modulus of GaTe nanosheets observed in the freestanding indentation tests, in figures 6(a) and (b) we show the deflection evolution of each component layer in the GaTe nanosheets during the indentation testing process. Generally speaking, it is found that during the whole indentation process the deflection of each component layer in the GaTe nanosheets is not synchronous. Taking the triple-layered GaTe nanosheets whose length is 33 nm for example (see figure 6(a)), the uppermost GaTe layer begins to deflect just after the indenter touches the GaTe nanosheets, while almost no deflections are initially found in the middle and lowermost layers. After the indentation depth increases to 1.5 nm, the middle layer begins to deflect. Furthermore, an obvious deflection is observed in the lowermost layer when the indentation depth is larger than 3.6 nm. Moreover, the deflection of the same component layer in the GaTe nanosheets with different layer counts and different lengths is different. Specifically, the component layer in the GaTe nanosheets having a smaller layer count and a larger

length tends to possess a larger deflection. The asynchronous deformation of different component layers in the GaTe nanosheets indicates that, there exists a significant interlayer compression in the GaTe nanosheets as shown in figure 6(c), which is in contrast to the assumptions of the existing beam and plate models. Actually, a similar interlayer compression phenomenon was also observed in recent nanoindentation simulations of freely suspended graphene sheets [22, 24, 25, 61]. The significant interlayer compression observed in freely suspended multilayer GaTe nanosheets indicates that the conventional continuum mechanical models, i.e. equations (1) and (2), widely used in the previous studies cannot precisely describe the freestanding indentation response of GaTe nanosheets. This could be the reason mainly responsible for the abnormal size-dependent Young's modulus of multilayer GaTe nanosheets obtained in the present freestanding indentation simulations and thus the extremely small Young's modulus gained from the above freestanding indentation experiments.

5. Multiple-beam (MB) and multiple-plate (MP) models for freestanding indentations of 2D materials

The conventional beam and plate theories widely used in describing the nanoindentation response of the freely suspended 2D materials (see equation (2)) require no thickness change of the 2D materials during the indentation process. However, as we illustrated above, in nanoindentation testing a significant interlayer compression is observed in the GaTe nanosheets due to the weak vdW interactions between their neighbouring component layers. Thus, the conventional beam and plate models are not accurate in describing the nanoindentation response of these freely suspended GaTe nanosheets. Moreover, the Euler–Bernoulli hypothesis used in the beam models (equation (2)) and the Kirchhoff hypothesis in the plate models (equation (1)) require the plane cross-section of a beam or a plate remain plane and keep perpendicular to the neutral axis or the mid-plane after deformation, which further requires no relative sliding between neighbouring component layers in the GaTe nanosheets. Under this circumstance, in the indented GaTe nanosheets the centre of their uppermost layer is expected to possess the largest compressive bending stress (strain), while the centre of their lowermost layer should have the largest tensile bending stress (strain). Between the uppermost and the lowermost layers the bending stress or the bending strain should change linearly and continuously along the thickness direction. However, as shown in figure 7(a), our MD results illustrate that the bending stress in the indented GaTe nanosheets changes discontinuously along the thickness direction, which indicates that the neighbouring component layers in the GaTe nanosheets are not bonded together tightly. In other words, there exists a significant interlayer shearing deformation in the indented GaTe nanosheets. The significant interlayer compression and interlayer shearing effects existing in the multilayer GaTe may result in the failure of conventional beam

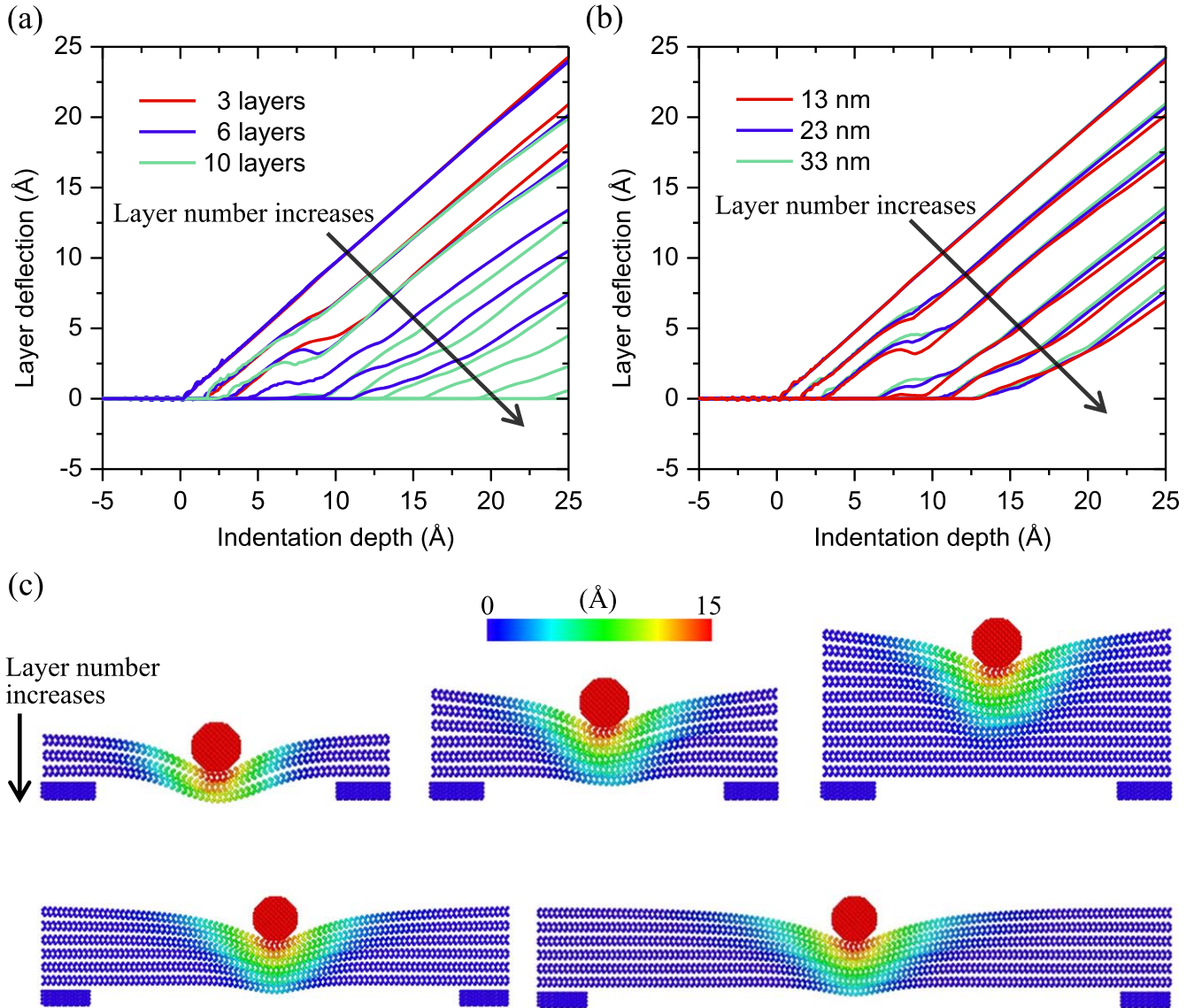


Figure 6. Deformations of the freely suspended GaTe nanosheets in nanoindentation simulations. (a), (b) Deflections of each component layer in the indented GaTe nanosheets with different layer counts and lengths. Here, each line corresponds to one component layer in the GaTe nanosheet. (c) Deformed configurations of the freely suspended GaTe nanosheets with different layer counts (top panel) and different lengths (bottom panel) when the same indentation depth of 15 nm is applied to them.

and plate models in describing the nanoindentation response of freely suspended GaTe nanosheets. Under this circumstance, we propose in the present study a more precise continuum mechanical model by considering these effects of interlayer interactions.

Firstly, we introduce the MB model as shown in figure 7(b), which can be utilised to describe the nanoindentation response of the freely suspended GaTe nanosheets indented by a cylindrical indenter. This novel MB model has the ability to take into account the effects of interlayer interactions (both the interlayer compression and the interlayer shearing effects) in the continuum mechanics analyses of the freestanding indentation testing of GaTe nanosheets. In the proposed MB model, each component layer in the GaTe nanosheets is treated as a beam model. Specifically, two ends of the lowermost beam are fixed, while the other component beams are allowed to deform freely.

To simulate the indentation load, a concentrated force is applied at the middle of the uppermost beam. An equivalent prestress is added in each component beam to represent the residual stress existing in the GaTe nanosheets. Moreover, similar to the previous studies on the multilayer graphene [62–66], BN [66, 67], MoS₂ [66] and vdW heterostructures [68], oblique springs are established between neighbouring beams to describe the interlayer shearing effect, while the interlayer compression effect is described by vertical springs in the MB model (see figure 7(b)).

Based on the MB model, the governing equation describing the nanoindentation response of the freely suspended GaTe nanosheets can be obtained through the minimum total potential energy principle. The statement of the variational principle can be mathematically represented as

$$\delta(U - W) = 0, \quad (3)$$

where U and W are the strain energy and the total work done

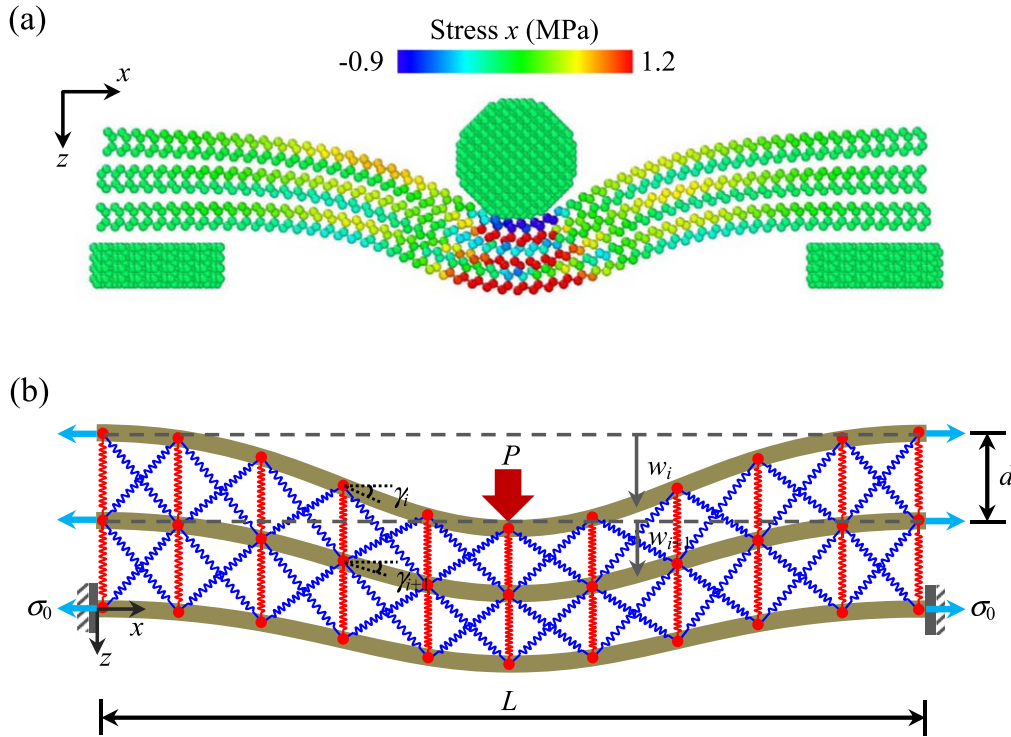


Figure 7. MB models for the nanoindentation of the freely suspended GaTe nanosheets. (a) Atomic stress distribution (stress in the x direction) of the indented GaTe nanosheets. (b) Schematic illustration of the newly proposed MB model. In the MB model each component layer in the GaTe nanosheets is treated as a beam model. Two adjacent beams are connected by the oblique springs (blue) and the vertical springs (red) to describe the interlayer shearing effect and the interlayer compression effect, respectively.

by external forces, respectively. The symbol δ indicates the variation.

As we illustrated above, the deformation in the indented GaTe nanosheets can originate from the deflection of their component GaTe layers and also the compression/shearing deformation of the vdW layers between the neighbouring vdW layer. If assuming that the shear strain in the vdW layer changes linearly along the thickness direction (i.e. z -axis shown in figure 7(b)), we can obtain the following expression of the shear strain: $\gamma_i = (w'_{i+1} - w'_i)(z/d) + (w'_{i+1} + w'_i)/2$. Thus, the strain energy component U_2 corresponding to the strain energy generated in the vdW layers of the multilayer GaTe nanosheets can be written as

$$U_1 = \frac{1}{2} \sum_{i=1}^n \int_0^L D(w''_i)^2 dx + \frac{1}{2} \sum_{i=1}^n \int_0^L \sigma_0 d(w'_i)^2 dx. \quad (4)$$

Here, D is the bending stiffness of the monolayer GaTe; d is the thickness of an individual component GaTe layer, which is assumed to equal to the interlayer spacing; w_i is the transverse displacement of the i th component layer; the superscript ($'$) denotes the derivative along the axial coordinate x .

The strain energy generated in the vdW layers can originate from both the interlayer compression and the interlayer shearing

deformations. Specifically, the interlayer compression may result in a compressive strain $\varepsilon_i = (w_{i+1} - w_i)/d$ in the vdW layer between the i th and the $i+1$ th component layers. In addition, the relative sliding between these two component layers in the multilayer GaTe also induces a shear strain in the corresponding vdW layer. If assuming that the shear strain in the vdW layer changes linearly along the thickness direction (i.e. z -axis shown in figure 7(b)), we can obtain the following expression of the shear strain: $\gamma_i = (w'_{i+1} - w'_i)(z/d) + (w'_{i+1} + w'_i)/2$. Thus, the strain energy component U_2 corresponding to the strain energy generated in the vdW layers of the multilayer GaTe nanosheets can be written as

$$U_2 = \frac{1}{2} \sum_{i=1}^{n-1} \int_0^L \int_{-d/2}^{d/2} c_{33} \frac{(w_{i+1} - w_i)^2}{d^2} dz dx + \frac{1}{2} \sum_{i=1}^{n-1} \int_0^L \int_{-d/2}^{d/2} c_{44} \frac{(w'_{i+1} + w'_i)^2}{4} dz dx, \quad (5)$$

where c_{33} and c_{44} are the interlayer compressive modulus and the interlayer shear modulus, respectively.

Meanwhile, as shown in figure 7(b), the total work W done by an indentation load $q(x) = P\delta(x-L/2)$ with δ being the Dirac delta function can be expressed as

$$W = \int_0^L q w_1 dx \quad (6)$$

Substituting equations (4)–(6) into equation (3), we can obtain

$$\begin{aligned} \delta(U - W) = & \sum_{i=1}^n \int_0^L Dw''_i \delta w'_i dx + \sum_{i=1}^n \int_0^L \sigma_0 dw'_i \delta w'_i dx \\ & + \sum_{i=1}^{n-1} \int_0^L c_{33} \frac{w_{i+1} - w_i}{d} \delta(w_{i+1} - w_i) dx \\ & + \sum_{i=1}^{n-1} \int_0^L c_{44} \frac{d}{4} (w'_{i+1} + w'_i) \delta(w'_{i+1} + w'_i) dx \\ & - \int_0^L q \delta w_1 dx = \int_0^L \left[Dw''''_1 - \sigma_0 dw''_1 - \frac{c_{33}}{s} (w_2 - w_1) \right. \\ & \left. - \frac{c_{44}s}{4} (w''_2 + w''_1) - q \right] \delta w_1 dx \\ & + \left[-Dw''''_1 + \sigma_0 dw''_1 + \frac{c_{44}d}{4} (w'_2 + w'_1) \right] \delta w_1 \Big|_0^L \\ & + Dw''_1 \delta w'_1 \Big|_0^L + \sum_{i=2}^{n-1} \int_0^L [Dw''''_i - \sigma_0 dw''_i] \delta w_i dx \\ & + \frac{c_{33}}{d} (2w_i - w_{i-1} - w_{i+1}) - \frac{c_{44}s}{d} (2w''_i + w''_{i-1} + w''_{i+1}) \Big] \\ & + \sum_{i=2}^{n-1} \left[-Dw''''_i + \sigma_0 dw''_i + \frac{c_{44}d}{4} (2w'_i + w'_{i-1} + w'_{i+1}) \right] \delta w_i \Big|_0^L \\ & + \sum_{i=2}^{n-1} Dw''_i \delta w'_i \Big|_0^L + \int_0^L \left[Dw''''_n - \sigma_0 dw''_n + \frac{c_{33}}{d} (w_n - w_{n-1}) \right. \\ & \left. - \frac{c_{44}d}{4} (w''_n + w''_{n-1}) \right] \delta w_n dx + [-Dw''''_n + \sigma_0 dw''_n \\ & + \frac{c_{44}d}{4} (w'_n + w'_{n-1})] \delta w_n \Big|_0^L + Dw''_n \delta w'_n \Big|_0^L = 0. \end{aligned} \tag{7}$$

Considering the arbitrariness of δw_i ($i = 1, 2, \dots, n$) in equation (7), we can obtain the following governing equations for the nanoindentation response of multilayer GaTe nanosheets from their MB models

$$\begin{aligned} Dw''''_1 - \sigma_0 dw''_1 - \frac{c_{33}}{d} (w_2 - w_1) - \frac{c_{44}d}{4} (w''_2 + w''_1) \\ - P \delta(x - L/2) = 0, \end{aligned} \tag{8.1}$$

$$\begin{aligned} Dw''''_i - \sigma_0 dw''_i + \frac{c_{33}}{d} (2w_i - w_{i-1} - w_{i+1}) \\ - \frac{c_{44}d}{4} (2w''_i + w''_{i-1} + w''_{i+1}) = 0, \quad i = 2, 3, \dots, n - 1, \end{aligned} \tag{8.2}$$

$$\begin{aligned} Dw''''_n - \sigma_0 dw''_n + \frac{c_{33}}{d} (w_n - w_{n-1}) - \frac{c_{44}d}{4} (w''_n + w''_{n-1}) = 0. \end{aligned} \tag{8.3}$$

Similarly, the following boundary conditions also can be obtained from equation (7)

$$-Dw''''_1 + \sigma_0 dw''_1 + \frac{c_{44}d}{4} (w'_2 + w'_1) \text{ or } w_1, Dw''_1 \text{ or } w'_1, \tag{9.1}$$

$$\begin{aligned} -Dw''''_i + \sigma_0 dw''_i + \frac{c_{44}d}{4} (2w'_i + w'_{i-1} + w'_{i+1}) \text{ or } w_i, \\ Dw''_i \text{ or } w'_i, \quad i = 2, 3, \dots, n - 1, \end{aligned} \tag{9.2}$$

$$-Dw''''_n + \sigma_0 dw''_n + \frac{c_{44}d}{4} (w'_n + w'_{n-1}) \text{ or } w_n, Dw''_n \text{ or } w'_n. \tag{9.3}$$

As for the freely suspend multilayer GaTe nanosheets considered in the nanoindentation tests shown in figure 7(b), their specific boundary conditions can be expressed as

$$-Dw''''_1 + \sigma_0 dw''_1 + \frac{c_{44}d}{4} (w'_2 + w'_1) = 0 \text{ and } w''_1 = 0, \tag{10.1}$$

$$\begin{aligned} -Dw''''_i + \sigma_0 dw''_i + \frac{c_{44}d}{4} (2w'_i + w'_{i-1} + w'_{i+1}) = 0 \\ \text{and } w''_i = 0, \quad i = 2, 3, \dots, n - 1, \end{aligned} \tag{10.2}$$

$$w_n = 0 \text{ and } w'_n = 0, \tag{10.3}$$

which are prescribed at the boundaries $x = 0$ and $x = L$.

The analytical solution of equation (8) satisfying the boundary conditions in equation (10) is usually hard to obtain. Thus, the differential quadrature (DQ) method was employed as an alternative method to obtain the numerical solutions of equation (8). In the DQ method, the derivative of a function with respect to a space variable at a given point is approximately treated as a weighted linear sum of the function values at all discrete points in that domain. Based on this idea, after generally noting the deformation function $w_i(x)$ of a component layer in GaTe nanosheets as the function $F(x)$, and discretising each component layer ($0 < x < L$) by N points, we can rewrite the derivative of the function $F(x)$ with respect to the axial coordinate x at the k th point (x_i) as follows

$$\frac{d^m F(x_i)}{dx^m} = \sum_{j=1}^N A_{ij}^{(m)} F(x_j), \tag{11}$$

where $A_{ij}^{(m)}$ is the weighting coefficients for the m th order derivative [69]. After employing the DQ method (equation (11)) to equation (8), we can achieve the discretised forms of the governing equation at the point $X_i = x_i/L$. Taking the uppermost component layer in the GaTe nanosheets as a typical example, we show below in equation (12) the discretised form of its governing equation, i.e. equation (8.1). For the complete discretised forms of the governing equations of the entire GaTe nanosheets, the readers can refer to the

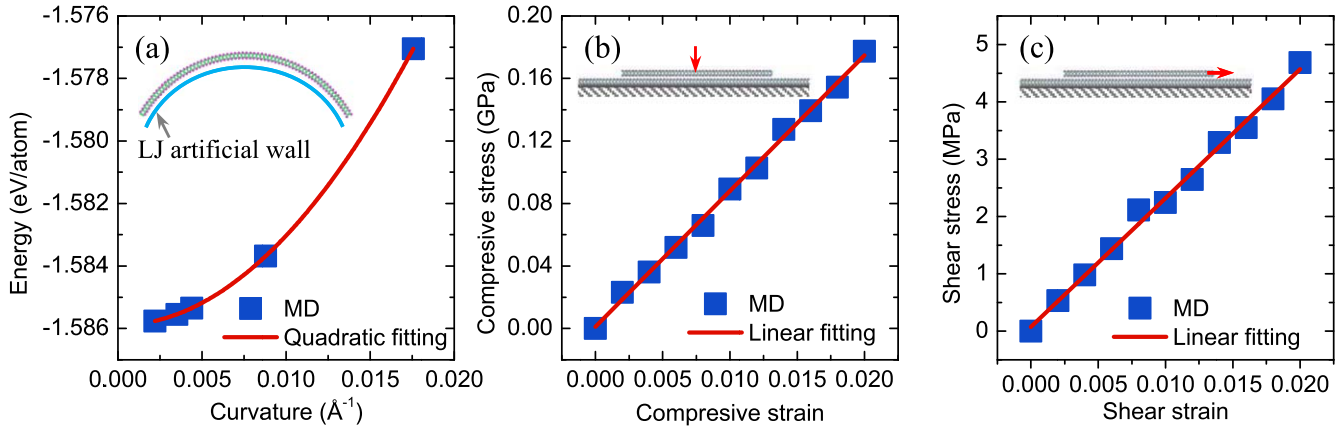


Figure 8. Bending stiffness and interlayer properties of the GaTe nanosheets obtained from MD simulations. (a) Potential energy as a function of the curvature for the bent monolayer GaTe. The bending stiffness can be achieved by applying a quadratic curve fitting to the obtained MD data. (b) Interlayer compressive stress as a function of the compressive strain in the double-layered GaTe. (c) Interlayer shear stress as a function of the shear strain in the double-layered GaTe. The interlayer compressive modulus and the interlayer shear modulus can be obtained by applying a linear curve fitting to the stress–strain curves obtained from MD simulations. Here, the insets show the corresponding setups employed in MD simulations.

supplementary materials:

$$\begin{aligned}
 & \frac{D}{L^4} \sum_{j=1}^N A_{ij}^{(4)} w_1(X_j) - \frac{\sigma_0 d}{L^2} \sum_{j=1}^N A_{ij}^{(2)} w_1(X_j) \\
 & - \frac{c_{33}}{d} [w_2(X_j) - w_1(X_j)] \\
 & - \frac{c_{44} d}{4L^2} \sum_{j=1}^N A_{ij}^{(2)} [w_1(X_j) + w_2(X_j)] \\
 & - P \delta \left(X_j - \frac{1}{2} \right) = 0.
 \end{aligned} \quad (12)$$

Similarly, after applying the DQ method to equation (11) we can obtain the discretised forms of the boundary conditions. The assemblage of the obtained discretised forms of the governing equations and the boundary conditions results in an overall linear algebraic system for the MB model of the GaTe nanosheets, which can be written as follows:

$$[K]\{w\} = \{P\}, \quad (13)$$

where $[K]$ is the global stiffness matrix of the MB system, $\{w\}$ is the global displacement vector, and $\{P\}$ is the global load vector. Equation (13) can be solved by using a solver of the linear algebraic system, which can be implemented with the aid of any mathematical software.

We can clearly see from equations (8) and (10) that there exist three material parameters, i.e. the bending stiffness D , the interlayer compressive modulus c_{33} and the interlayer shear modulus c_{44} needed to be identified before we can use the MB model to quantitatively describe the freestanding indentation response of the GaTe nanosheets. In the present study, the values of all these material parameters were extracted from MD simulations. Specifically, following the previous MD studies on calculating the bending stiffness of various nanomaterials [70, 71], the bending stiffness of the monolayer GaTe can be obtained by imposing different curvatures to the bent monolayer GaTe. In doing this, a square

monolayer GaTe nanosheet with a size of $10 \text{ nm} \times 10 \text{ nm}$ was completely bounded to an idealised surface with the wall-atom interactions as shown in the inset of figure 8(a), which was described by the LJ 9-3 potential. Here, the values of the parameters in the LJ potential were properly chosen to make sure that the GaTe nanosheet can well adhere to the virtual surface. Through changing the radius of the virtual surface, we can bend the GaTe nanosheet with different curvatures. The energy of the bent GaTe nanosheets changing with the bending curvature obtained from MD simulations is shown in figure 8(a). Meanwhile, in view of the continuum mechanics, the elastic bending energy U_b generated in a continuum elastic model bent with a curvature κ can be expressed as $U_b = DS\kappa^2/2$, where S is the area of the structure. Thus, by fitting this expression to the MD results shown in figure 8(a) we can obtain the bending stiffness $D = 15 \text{ eV}$ for the monolayer GaTe, which agrees well with the value of 14 eV extracted from the previous first principles calculations [72]. To calculate the interlayer compressive modulus and the interlayer shear modulus from MD simulations, we initially created a GaTe monolayer with a size of $30 \text{ nm} \times 30 \text{ nm}$, which was treated as a substrate by freezing all atoms in it. Afterwards, another GaTe monolayer with a size of $10 \text{ nm} \times 10 \text{ nm}$ was built above this GaTe substrate. In calculating the interlayer compressive modulus, the suspended GaTe monolayer was gradually moved towards to its bottom GaTe substrate (see the inset of figure 8(b)), which results in a compressive strain generated in the vdW layer between these two GaTe monolayers. In response to the approach of these two GaTe monolayers, a repulsive stress is produced in the suspended GaTe monolayer, which is found to linearly increase as the compressive strain grows (see figure 8(b)). Thus, after applying a linear curve fitting to the obtained stress–strain curve shown in figure 8(b), we obtained the interlayer compressive modulus $c_{33} = 8.76 \text{ GPa}$. Similarly, to calculate the interlayer shear modulus we created a shear

strain in the vdW layer by moving the suspended GaTe monolayer with an in-plane displacement as shown in the inset of figure 8(c). As a result of the in-plane movement of the suspended GaTe monolayer, a shear stress will be generated in the vdW layer, which, as shown in figure 8(c), shows a linear relationship with the shear strain. Thus, the interlayer shear modulus can be represented by the slope of the stress–strain curve shown in figure 8(c), which is $c_{44} = 0.24$ GPa.

After solving equation (13) together with the values of the material parameters D , c_{33} and c_{44} extracted above, we can obtain the indentation response of the freely suspended multilayer GaTe nanosheets from their MB models. Similar to the MD results, a linear relationship is observed between the indentation depth and the applied indentation load (results are not shown here). Thus, after fitting equation (2) to the obtained indentation depth-indentation load curves, we can gain the effective Young's modulus of the GaTe nanosheets from their MB models, which is graphically shown in figures 5(c) and (d). Here, the GaTe nanosheets considered in the present MB models have a geometric size the same as those considered in the above MD simulations. We can see from figures 5(c) and (d) that the MB results agree well with the MD results, which indicates that the vdW interaction between the neighbouring layers in the multilayer GaTe nanosheets plays a crucial role in determining their freestanding indentation responses and thus should be considered in the continuum mechanical models describing their nanoindentation behaviours. Moreover, in comparison with other 2D materials such as the multilayer graphene, BN, and MoS₂, the present multilayer GaTe is found to possess relatively small interlayer compressive modulus and interlayer shear modulus [67, 73, 74]. This fact suggests that the interlayer interactions may have a more significant influence on the mechanical behaviours of multilayer GaTe nanosheets when compared to some other 2D materials. This strong effect of interlayer interactions in the multilayer GaTe is thus majorly responsible for the significant size-dependent Young's modulus observed in the freestanding indentation tests of the multilayer GaTe nanosheets and is thus the main reason for the extremely small Young's modulus detected in the relatively thick GaTe nanosheets.

It is noted that the above MB models are developed for the GaTe nanosheets indented by a cylindrical indenter, in which each component layer can be described by a beam model. However, as for the GaTe nanosheets indented by an indenter with a spherical shape analogous to the shape of the AFM or the Berkovich indenter tip, their component layers should be modelled by a plate model rather than a beam model. Under this circumstance, an MP model should be introduced to describe the nanoindentation behaviours of the freely suspended multilayer GaTe nanosheets. In doing this, the similar treatment employed above in developing the MB models (i.e. the minimum total potential energy principle) is further extended to obtain the MP model for the multilayer GaTe nanosheets. After an indentation load is applied to the centre of the uppermost component layer in the multilayer GaTe nanosheets, in the MP model the governing equations

characterising the freestanding indentation behaviours of the entire GaTe nanosheets can be written as follows (the derivation details are described in the supplementary materials):

$$\begin{aligned} D\nabla^4 w_1 - \sigma_0 d \nabla^2 w_1 - \frac{c_{33}}{d}(w_2 - w_1) \\ - \frac{c_{44}d}{4} \nabla^2 (w_1 + w_2) \\ - P\delta(x - L/2)\delta(y - w/2) = 0, \end{aligned} \quad (14.1)$$

$$\begin{aligned} D\nabla^4 w_i - \sigma_0 d \nabla^2 w_i + \frac{c_{33}}{d}(2w_i - w_{i-1} - w_{i+1}) \\ - \frac{c_{44}d}{4} \nabla^2 (2w_i + w_{i-1} + w_{i+1}) = 0, \quad i = 2, 3, \dots, n-1, \end{aligned} \quad (14.2)$$

$$\begin{aligned} D\nabla^4 w_n - \sigma_0 d \nabla^2 w_n + \frac{c_{33}}{d}(w_n - w_{n-1}) \\ - \frac{c_{44}d}{4} \nabla^2 (w_n + w_{n-1}) = 0, \end{aligned} \quad (14.3)$$

where x and y axes are defined along the length and the width directions of the component GaTe layer, respectively. Moreover, in equation (14) $\nabla^2 = \partial^2/\partial x^2 + \partial^2/\partial y^2$ is the 2D Laplace operator and thus $\nabla^4 = \partial^4/\partial x^4 + 2\partial^4/\partial x^2\partial y^2 + \partial^4/\partial y^4$.

The corresponding boundary conditions for each component layer in the indented GaTe nanosheets can be mathematically described by the following equations:

$$\begin{aligned} -D\frac{\partial^3 w_1}{\partial x^3} + \sigma_0 d \frac{\partial w_1}{\partial x} + \frac{c_{44}d}{4} \left(\frac{\partial w_2}{\partial x} + \frac{\partial w_1}{\partial x} \right) \text{ or } w_1, \\ D\frac{\partial^2 w_1}{\partial x^2} \text{ or } \frac{\partial w_1}{\partial x}, \end{aligned} \quad (15.1)$$

$$\begin{aligned} -D\frac{\partial^3 w_i}{\partial x^3} + \sigma_0 d \frac{\partial w_i}{\partial x} + \frac{c_{44}d}{4} \left(2\frac{\partial w_i}{\partial x} + \frac{\partial w_{i-1}}{\partial x} + \frac{\partial w_{i+1}}{\partial x} \right) \\ \text{ or } w_i, D\frac{\partial^2 w_i}{\partial x^2} \text{ or } \frac{\partial w_i}{\partial x}, \quad i = 2, 3, \dots, n-1, \end{aligned} \quad (15.2)$$

$$\begin{aligned} -D\frac{\partial^3 w_n}{\partial x^3} + \sigma_0 d \frac{\partial w_n}{\partial x} + \frac{c_{44}d}{4} \left(\frac{\partial w_n}{\partial x} + \frac{\partial w_{n-1}}{\partial x} \right) \text{ or } w_n, \\ D\frac{\partial^2 w_n}{\partial x^2} \text{ or } \frac{\partial w_n}{\partial x}, \end{aligned} \quad (15.3)$$

which are prescribed at the boundaries $x = 0$ and $x = L$. At the boundaries $y = 0$ and $y = w$, the expressions of the boundary conditions are similar to equation (15) except that the derivative of the displacement functions $w_i(x, y)$ ($i = 1, 2, \dots, n$) now is along the coordinate y rather than x . After determining the specific boundary conditions of the multilayer GaTe nanosheets tested in a specific freestanding indentation experiment, together with these specific boundary conditions we can achieve their nanoindentation response from their MP models based on equation (14) solved by some numerical methods such as the DQ method we introduced above.

6. Conclusions

In this paper the nanoindentation behaviours of the freely suspended multilayer GaTe nanosheets are investigated by a method combining experimental testing, computational simulations and theoretical modelling. In the previous freestanding indentation tests of ultrathin 2D materials with one layer or a few layers, their Young's modulus is usually extracted from the stretching stage during the indentation process. However, the present freestanding indentation tests of multilayer GaTe nanosheets with a relatively large thickness indicate that the stretching stage is not accurate in determining their Young's modulus. This is because the stretching deformation in thick 2D materials becomes dominant only when a relatively large indentation load is applied onto them, which, however, may cause severe plastic deformations accompanied with the stretching response. Under this circumstance, the bending stage in the indentation process should be alternatively employed to quantify the Young's modulus of thick 2D materials. In combination with the existing continuum mechanical models and FE simulations, a relatively small Young's modulus is obtained from the freestanding indentation tests of the multilayer GaTe nanosheets, which is two orders of magnitude smaller than the value obtained from DFT calculations.

MD-based nanoindentation simulations are conducted to the freely suspended multilayer GaTe nanosheets to explain the difference between the nanoindentation experiments and DFT calculations. Our simulation results show that the Young's modulus of GaTe nanosheets strongly depends on their geometric size. Specifically, the Young's modulus of GaTe nanosheets is found to decrease as their thickness (or layer count) increases but increase as their length increases. The significant elastic softening of GaTe nanosheets with increasing thickness ultimately results in the extremely small Young's modulus observed in the nanoindentation experiments of the relatively thick GaTe nanosheets. This size-dependent Young's modulus observed in the nanoindentation experiments and simulations, however, is contrast to the nearly constant Young's modulus detected in DFT calculations on the GaTe nanosheets with different layer counts.




Our MD simulations further reveal that the size-dependent Young's modulus of GaTe nanosheets observed in the freestanding indentation tests is induced by the synergistic effects of interlayer compression and interlayer shearing. These significant effects of interlayer interactions, however, are ignored in the conventional continuum mechanical models widely used in the previous studies. To overcome the limitation of these existing continuum mechanical models, we propose here novel MB and MP models, which can take into account the effects of interlayer interactions in the continuum modelling of the freestanding indentation tests of 2D materials. The results extracted from these new models are found to agree well with the MD results without any additional parameters fitting. Overall, the outcomes of this work not only present a comprehensive understanding of the mechanical behaviours of the newly synthesised 2D GaTe nanosheets, but also provide a more precise continuum mechanical model in

describing the nanoindentation responses of freely suspended 2D materials.

Acknowledgments

This work was supported by the National Natural Science Foundation of China (No. 11602074). J Z also acknowledges the financial support from Harbin Institute of Technology (Shenzhen Graduate School) through the Scientific Research Starting Project for New Faculty.

ORCID iDs

Jin Zhang  <https://orcid.org/0000-0001-8796-2306>
 Penghua Ying  <https://orcid.org/0000-0002-5758-2369>
 Huarui Sun  <https://orcid.org/0000-0003-1429-0611>

References

- [1] Novoselov K S, Geim A K, Morozov S V, Jiang D, Zhang Y, Dubonos S V, Grigorieva I V and Firsov A A 2004 *Science* **306** 666–9
- [2] Golberg D, Bando Y, Huang Y, Terao T, Mitome M, Tang C and Zhi C 2010 *ACS Nano* **4** 2979–93
- [3] Cao T *et al* 2012 *Nat. Commun.* **3** 887
- [4] Vogt P, De Padova P, Quaresima C, Avila J, Frantzeskakis E, Asensio M C, Resta A, Ealet B and Le Lay G 2012 *Phys. Rev. Lett.* **108** 155501
- [5] Li L K, Yu Y J, Ye G J, Ge Q Q, Ou X D, Wu H, Feng D L, Chen X H and Zhang Y B 2014 *Nat. Nanotechnol.* **9** 372–7
- [6] Tan C *et al* 2017 *Chem. Rev.* **117** 6225–331
- [7] Zhang H, Chhowalla M and Liu Z F 2018 *Chem. Soc. Rev.* **47** 3015–7
- [8] Akinwande D *et al* 2017 *Extreme Mech. Lett.* **13** 42–77
- [9] Zhan H, Guo D and Xie G X 2019 *Nanoscale* **11** 13181–212
- [10] Kim J H, Jeong J H, Kim N, Joshi R and Lee G H 2019 *J. Phys. D: Appl. Phys.* **52** 083001
- [11] Desai S B, Seol G, Kang J S, Fang H, Battaglia C, Kapadia R, Ager J W, Guo J and Javey A 2014 *Nano Lett.* **14** 4592–7
- [12] Qi J S, Qian X F, Qi L, Feng J, Shi D N and Li J 2012 *Nano Lett.* **123** 1224–8
- [13] Lee C G, Wei X D, Kysar J W and Hone J 2008 *Science* **321** 385–8
- [14] Lee G H *et al* 2013 *Science* **340** 1073–6
- [15] Cao G X and Gao H J 2019 *Prog. Mater. Sci.* **103** 558–95
- [16] Yang Y C *et al* 2017 *Adv. Mater.* **29** 1604201
- [17] Li X, Sun M, Shan C X, Chen Q and Wei X L 2018 *Adv. Mater. Interfaces* **5** 1701246
- [18] Bunch J S, van der Zande A M, Verbridge S S, Frank I W, Tanenbaum D M, Parpia J K, Craighead H G and McEuen P L 2007 *Science* **315** 490–3
- [19] Chitara B and Ya'akovitz A 2017 *Nanotechnology* **28** 42LT02
- [20] Han J, Ryu S and Sohn D 2016 *Carbon* **107** 310–8
- [21] Sun Y F *et al* 2019 *Nano Lett.* **19** 761–9
- [22] Han J, Ryu S, Kim D K, Woo W and Sohn D 2016 *Europhys. Lett.* **114** 68001
- [23] Falin A *et al* 2017 *Nat. Commun.* **8** 15815
- [24] Zhong T, Li J B and Zhang K W 2019 *J. Appl. Phys.* **125** 175110

- [25] Huo Z L, Guo Z R, Leng J T and Chang T C 2019 *Sci. China Tech. Sci.* **62** 269–75
- [26] Gómez-Navarro C, Burghard M and Kern K 2008 *Nano Lett.* **8** 2045–9
- [27] Li C, Bando Y, Zhi C Y, Huang Y and Golberg D 2009 *Nanotechnology* **20** 385707
- [28] Bertolazzi S, Brivio J and Kis A 2011 *ACS Nano* **5** 9703–9
- [29] Chitara B and Ya'akovovitz A 2018 *Nanoscale* **10** 13022–7
- [30] Wang J Y, Li Y, Zhan Z Y, Li T, Zhen L and Xu C Y 2016 *Appl. Phys. Lett.* **108** 013104
- [31] Tu Q, Spanopoulos I, Yasaei P, Stoumpos C C, Kanatzidis M G, Shekhawat G S and Dravid V P 2018 *ACS Nano* **12** 10347–54
- [32] Kumar R and Parashar A 2016 *Nanoscale* **8** 22–49
- [33] Liu F, Shimotani H, Shang H, Kanagasekaran T, Zólyomi V, Drummond N, Fal'ko V I and Tanigaki K 2014 *ACS Nano* **8** 752–60
- [34] Huang S X et al 2016 *ACS Nano* **10** 8964–72
- [35] Antonius G, Qiu D Y and Louie S G 2018 *Nano Lett.* **18** 1925–9
- [36] Zhao Q et al 2016 *Phys. Chem. Chem. Phys.* **18** 18719–26
- [37] Yu Y W, Ran M, Zhou S S, Wang R Y, Zhou F Y, Li H Q, Gan L, Zhu M Q and Zhai T Y 2019 *Adv. Funct. Mater.* **29** 1901012
- [38] Li Y H et al 2019 *Nanotechnology* **30** 335703
- [39] Suk J W, Piner R D, An J and Ruoff R S 2010 *ACS Nano* **4** 6557–64
- [40] Begley M R and Mackin T J 2004 *J. Mech. Phys. Solids* **52** 2005–23
- [41] Timoshenko S and Woinowsky-Krieger S 1959 *Theory of Plates and Shells* 2nd edn (New York: McGraw-Hill)
- [42] Clark S J, Segall M D, Pickard C J, Hasnip P J, Probert M J, Refson K and Payne M C 2005 *Z. Kristallogr.* **220** 567–70
- [43] Perdew J P, Burke K and Ernzerhof M 1996 *Phys. Rev. Lett.* **77** 3865–8
- [44] Grimme S 2006 *J. Comput. Chem.* **27** 1787–99
- [45] Mortazavi B, Rahaman O, Dianat A and Rabczuk T 2016 *Phys. Chem. Chem. Phys.* **18** 27405–13
- [46] Hu L, Huang X R and Wei D S 2017 *Phys. Chem. Chem. Phys.* **19** 11131–41
- [47] Shenoy U S, Gupta U, Narang D S, Late D J, Waghmare U V and Rao C N R 2016 *Chem. Phys. Lett.* **651** 148–54
- [48] Olmos-Asar J A, Leão C R and Fazzio A 2018 *J. Appl. Phys.* **124** 045104
- [49] Zhou L X, Wang Y G and Cao G X 2013 *J. Phys.: Condens. Matter* **25** 475301
- [50] Stillinger F H and Weber T A 1985 *Phys. Rev. B* **31** 5262–71
- [51] Jiang J W 2017 *Handbook of Stillinger-Weber Potential Parameters for Two-Dimensional Atomic Crystals* (London: IntechOpen Limited)
- [52] Stuart S J, Tutein A B and Harrison J A 2000 *J. Chem. Phys.* **112** 6472–86
- [53] Tersoff J 1989 *Phys. Rev. B* **39** 5566–8
- [54] Munetoh S, Motooka T, Moriguchi K and Shintani A 2007 *Comput. Mater. Sci.* **39** 334–9
- [55] Chandrachud P 2015 *J. Phys.: Condens. Matter* **27** 445502
- [56] Kinney K E and Bartell L S 1996 *J. Phys. Chem. C* **100** 15416–20
- [57] Rappé A K, Casewit C J, Colwell K S, Goddard W A III and Skiff W M 1992 *J. Am. Chem. Soc.* **114** 10024–35
- [58] Plimpton S J 1995 *J. Comput. Phys.* **117** 1–19
- [59] Nosé S 1984 *J. Chem. Phys.* **81** 511–9
- [60] Pruessner M W, King T T, Kelly D P, Grover R, Calhoun L C and Ghodssi R 2003 *Sensors Actuators A* **105** 190–200
- [61] Zhou L X, Wang Y G and Cao G X 2013 *Carbon* **57** 357–62
- [62] Liu Y L, Xu Z P and Zheng Q S 2011 *J. Mech. Phys. Solids* **59** 1613–22
- [63] Shen Y K and Wu H A 2012 *Appl. Phys. Lett.* **100** 101909
- [64] Peng S Y and Wei Y J 2016 *J. Mech. Phys. Solids* **92** 278–96
- [65] Pan F, Wang G R, Liu L Q, Chen Y L, Zhang Z and Shi X H 2019 *J. Mech. Phys. Solids* **122** 340–63
- [66] Wang G R, Dai Z H, Xiao J K, Feng S Z, Weng C X, Liu L Q, Xu Z P, Huang R and Zhang Z 2019 *Phys. Rev. Lett.* **123** 116101
- [67] Zhang J and Zhou J L 2018 *Nanotechnology* **29** 395703
- [68] Zhang J 2019 *J. Appl. Phys.* **125** 025113
- [69] Shu C 2000 *Differential Quadrature and Its Application in Engineering* (New York: Springer)
- [70] Roman R E, Kwan K and Cranford S W 2015 *Nano Lett.* **15** 1585–90
- [71] Liu X, Zhang G and Zhang Y W 2015 *J. Phys. Chem. C* **119** 24156–64
- [72] Demirci S, Avazlı N, Durgun E and Cahangirov S 2017 *Phys. Rev. B* **95** 115409
- [73] Hajgató B, Güryel S, Dauphin Y, Blairon J M, Miltner H E, Van Lier G, De Proft F and Geerlings P 2013 *Chem. Phys. Lett.* **564** 37–40
- [74] Peelaers H and Van de Walle C G 2014 *J. Phys. Chem. C* **118** 12073–6